NEOPLASIA
www.neoplasia.com

Volume 13 Number 3 March 2011 pp. 244–253 244

Vascular Profile Characterization of Liver Tumors by Magnetic Resonance Imaging Using Hemodynamic Response Imaging in Mice[1,2]

Yifat Edrei[*,†,3], Eitan Gross[‡,3], Nathalie Corchia[*], Galia Tsarfaty[§], Eithan Galun[*], Orit Pappo[¶] and Rinat Abramovitch[*,†]

*The Goldyne Savad Institute for Gene Therapy, Hadassah Hebrew University Medical Center, Jerusalem, Israel; [†]MRI/MRS Laboratory HBRC, Hadassah Hebrew University Medical Center, Jerusalem, Israel; [‡]Department of Pediatric Surgery, Hadassah Hebrew University Medical Center, Jerusalem, Israel; [§]Department of Radiology, Sheba Medical Center, Tel Hashomer, Israel; [¶]Department of Pathology, Hadassah Hebrew University Medical Center, Jerusalem, Israel

Abstract

Recently, we have demonstrated the feasibility of using hemodynamic response imaging (HRI), a functional magnetic resonance imaging (MRI) method combined with hypercapnia and hyperoxia, for monitoring vascular changes during liver pathologies without the need of contrast material. In this study, we evaluated HRI ability to assess changes in liver tumor vasculature during tumor establishment, progression, and antiangiogenic therapy. Colorectal adenocarcinoma cells were injected intrasplenically to model colorectal liver metastasis (CRLM) and the *Mdr2* knockout mice were used to model primary hepatic tumors. Hepatic perfusion parameters were evaluated using the HRI protocol and were compared with contrast-enhanced (CE) MRI. The hypovascularity and the increased arterial blood supply in well-defined CRLM were demonstrated by HRI. In CRLM-bearing mice, the entire liver perfusion was attenuated as the HRI maps were significantly reduced by 35%. This study demonstrates that the HRI method showed enhanced sensitivity for small CRLM (1-2 mm) detection compared with CE-MRI (82% *versus* 38%, respectively). In addition, HRI could demonstrate the vasculature alteration during CRLM progression (arborized vessels), which was further confirmed by histology. Moreover, HRI revealed the vascular changes induced by rapamycin treatment. Finally, HRI facilitates primary hepatic tumor characterization with good correlation to the pathologic differentiation. The HRI method is highly sensitive to subtle hemodynamic changes induced by CRLM and, hence, can function as an imaging tool for understanding the hemodynamic changes occurring during CRLM establishment, progression, and antiangiogenic treatment. In addition, this method facilitated the differentiation between different types of hepatic lesions based on their vascular profile noninvasively.

Neoplasia (2011) 13, 244–253

Abbreviations: CE-MRI, contrast-enhanced MRI; CRLM, colorectal liver metastasis; fMRI, functional MRI; Gd-DTPA, gadolinium–diethylene-triaminepenta-acetate; HCC, hepatocellular carcinoma; HPF, high-power microscopic fields; HRI, hemodynamic response imaging; MRI, magnetic resonance imaging; RAPA, rapamycin; ROI, region of interest; SMA, smooth muscle actin; T_1W, T_1-weighted; T_2W, T_2-weighted; ΔS_{CO_2}, signal intensity change due to hypercapnia; ΔS_{O_2}, signal intensity change due to hyperoxia; VEGF, vascular endothelial growth factor

Address all correspondence to: Rinat Abramovitch, PhD, The Goldyne Savad Institute of Gene Therapy, Hadassah Hebrew University Medical Center, PO Box 12000, Jerusalem 91120, Israel. E-mail: rinat@hadassah.org.il

[1]This research was supported in part by grant number 1243/10 from the Israel Science Foundation (for R.A.) and by the Horwitz Foundation through The Center for Complexity Science (for R.A. and Y.E.).

[2]This article refers to supplementary materials, which are designated by Figures W1 and W2 and are available online at www.neoplasia.com.

[3]These authors contributed equally to this work.

Received 16 September 2010; Revised 2 December 2010; Accepted 8 December 2010

DOI 10.1593/neo.101354

Introduction

Hepatic tumors represent a major burden in the medical practice, considering their high incidence, the diagnostic difficulties, and the high rate of morbidity and mortality. Hepatocellular carcinoma (HCC) is the fifth most common cancer worldwide and the third most common cause of cancer-related mortality [1]. Nowadays, early stage HCC diagnosis is feasible in 30% to 60% of cases, thus enabling the application of curative strategies; however, timely and accurate diagnosis is of paramount importance [2]. The liver is also one of the most commonly involved organs in metastatic disease [3]. Colorectal cancer is the third most common cancer in the United States [4]. The development of colorectal liver metastases (CRLMs) is the main cause of death in these patients [5].

Early diagnosis is critical for successful resection and for refined treatment selection criteria in both liver pathologies [6,7]. Only a minority of CRLM patients (<20%) are amenable to resection [8–10]. Thus, alternative treatments are under investigation. Recently, considerable research has focused on the search for antiangiogenic therapies for CRLM. The immunosuppressant rapamycin (RAPA) is a highly specific inhibitor of mTOR that can further inhibit tumor growth [11], tumor progression [12], and metastasis [13] both through its antiangiogenic activity (by impairing the production of vascular endothelial growth factor [VEGF]) and direct inhibition of cell proliferation and cell cycle progression [14,15]. Tumor response to therapy is usually assessed by measurements of tumor size using morphologic imaging techniques. Because antiangiogenic therapies may not lead to substantial tumor mass reduction, their effect is better imaged using techniques designed to assess vascular function rather than the conventional measurements of tumor size [16–18]. Dynamic contrast-enhanced magnetic resonance imaging (CE-MRI) has been used previously to examine the acute and chronic effects of VEGF signaling inhibitors, both preclinically [19–21] and clinically [22,23]. However, the physiologic significance of these parameters can be complex, and there is currently no consensus as to the best parameters to be used or the most appropriate measurement and analysis method [24,25].

It is well known that, whereas the normal liver is supplied predominantly by the portal vein, in patients with overt hepatic tumor, a higher proportion of liver blood flow is derived from the hepatic artery [26,27]. Moreover, even small or occult lesions may lead to subtle changes in liver blood flow [28,29]. Therefore, monitoring hemodynamical changes using perfusion imaging may facilitate the characterization of the vascular profile, which can lead to earlier and more accurate detection of hepatic tumors. This strategy was recently endorsed by the European [30] and American Associations for the Study of the Liver [31].

Today, to acquire perfusion images, intravenous administration of a contrast agent is necessary. Multiphasic CE-MRI is currently accepted as a reliable method for detecting and characterizing liver tumors [32]. A good separation of arterial from portal venous phases requires short acquisition time, which leads to low spatial resolution or partial volume coverage. Recently, we demonstrated the feasibility of hemodynamic response imaging (HRI), a functional MRI (fMRI) method combined with hypercapnia and hyperoxia, for monitoring changes in liver perfusion and hemodynamics without the need of contrast agent administration [33,34]. We established its ability to image the hemodynamic changes occurring under different pathologic states such us liver fibrosis, acute bleeding, and during liver regeneration [34,35].

In the present study, we aimed to assess the use of HRI for the detection and characterization of the early vascular and perfusion changes occurring during CRLM establishment, for the study of the vascular changes in CRLM during antiangiogenic therapy, and for the assistance to characterize the vascular profile of primary hepatic tumors. We used the CT-26 murine colon carcinoma liver metastatic mouse model [36] and the *Mdr2* knockout mice [37] as the inflammation-induced primary liver tumor model. HRI utility for liver tumor diagnosis and vascular characterization was assessed in these animal models. The HRI results were compared with CE-MRI and were further confirmed by histology. HRI utility for antiangiogenic effect assessment was evaluated on CRLM-bearing mice that were treated with RAPA at a relevant dose. In this study, the HRI method showed high sensitivity for the vascular changes occurring in liver tumors in experimental animal models.

Materials and Methods

Animals

For the CRLM model, 7- to 8-week-old male CB6F1 mice were used (31 mice). For the HCC model, 12- to 18-month-old *Mdr2* knockout mice [37] were analyzed (21 lesions in 12 mice). All experiments were performed in accordance with the guidelines and approval of the Animal Care and Use Committee of the Hebrew University, which holds National Institutes of Health approval (OPRR-A01-5011).

Mouse Model of CRLM

CT-26 murine colorectal adenocarcinoma cells [36] were injected intrasplenically to anesthetized CB6F1 mice (10^4 cells in 300 μl per mouse). After 5 minutes, the spleens were removed, allowing the cells to enter the portal circulation and to initiate liver metastases. In this model, one to five hepatic nodules per mouse were detected by MRI 13 to 17 days after cell inoculation. In this animal model, the tumors appeared hyperintense in T_2-weighted (T_2W) images (Figure 1*A*). The presence of CRLM lesions was further verified by repeated MRI scans and histologic analysis. For HRI assessment, 47 lesions (1-5 mm in diameter) were examined, and for CE-MRI assessment, 42 lesions were analyzed. For antiangiogenic treatment surveillance, eight CRLM-bearing mice were treated with RAPA (Fermentek Ltd, Jerusalem, Israel) at a dosage of 2 mg/kg per day intraperitoneally. The treatment started on the day of tumor appearance as detected by MRI.

Magnetic Resonance Imaging

MRI experiments were performed using a horizontal 4.7-T Biospec spectrometer (Bruker Medical, Ettlingen, Germany) with a 3.5-cm birdcage coil. Mice were anesthetized with pentobarbital (30 mg/kg, intraperitoneally) and placed supine. Coronal and axial T_1-weighted (T_1W) spin-echo images were acquired for liver segmentation purposes (repetition time = 360 milliseconds, echo time = 18 milliseconds). Tumor assessment was done using T_2W fast spin-echo images (repetition time = 2000 milliseconds, echo time = 37 milliseconds, in-plane resolution = 117 μm, slice thickness = 1 mm).

Hemodynamic Response Imaging. Changes in hepatic hemodynamics were evaluated using the HRI protocol as previously described [33]. In brief, the images were acquired using T_2*-weighted gradient echo images (repetition time = 147 milliseconds, echo time = 10 milliseconds, field of view = 3 cm, in-plane resolution = 117 μm, slice thickness = 1 mm, 2 averages, 37 seconds per image) combined with

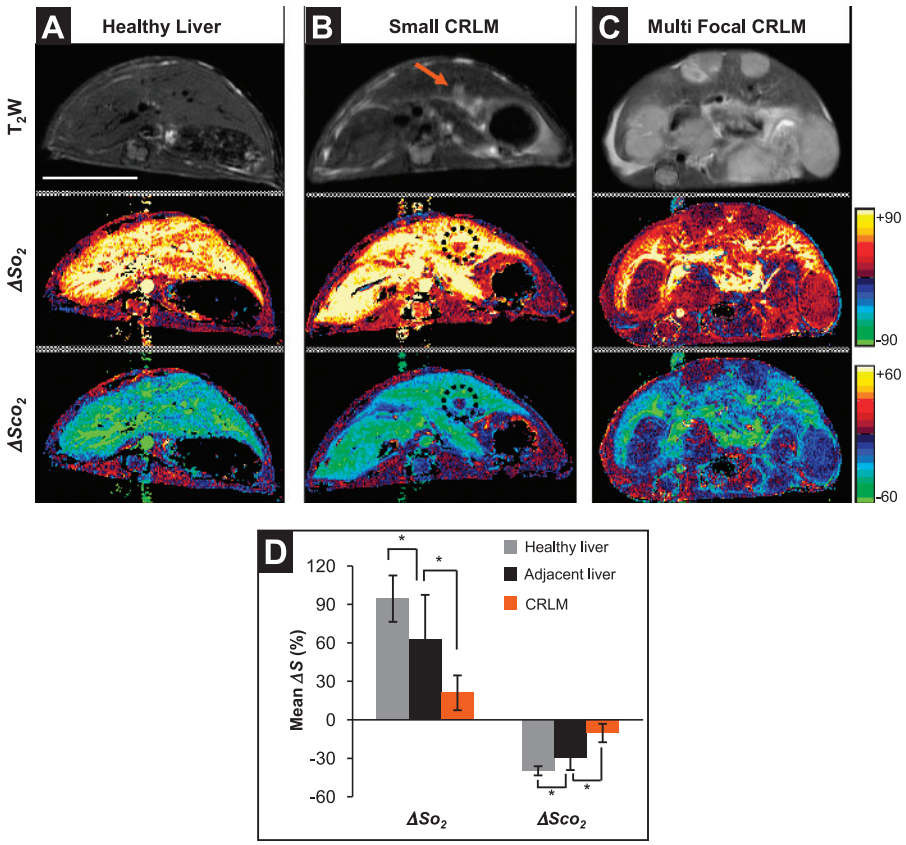

Figure 1. CRLM vasculature profile characterization by HRI: Representatives axial T_2W images (top) and ΔS_{O_2} (hyperoxia effect—center row) and ΔS_{CO_2} (hypercapnia effect—bottom) maps of healthy liver (A), small CRLM acquired during early phase (B, red arrow), and advanced multifocal CRLM (C). Bar = 1 cm. Color scales for ΔS maps are located on the right. The HRI method clearly highlighted CRLM from healthy liver tissue. (D) Mean ΔS_{O_2} and ΔS_{CO_2} values ± SD of healthy livers (n = 10) *versus* livers of CRLM-bearing mice (n = 10) and CRLM (n = 30). *P < .001.

breathing of air, air-CO_2 (5% CO_2, 4 L/min), and carbogen (95% O_2 + 5% CO_2, 4 L/min) through a homemade mask.

Contrast-Enhanced MRI. To compare HRI results to a standard method, CE-MRI was performed with T_1W FLASH sequence (repetition time = 34 milliseconds, echo time = 5 milliseconds, field of view = 3 cm, in-plane resolution = 117 μm, slice thickness = 1 mm, 1 average, 80 measurements), resulting in a temporal resolution of 4 seconds. After the 10th image, gadolinium–diethylene-triaminepenta-acetate (Gd-DTPA, Magnetol; Soreq Radiopharmaceuticals, Yavne, Israel; 0.5 M, 100 μl) was administered through the tail vein at a dose of 0.1 mmol Gd/kg. Signal intensity–time curves and multiphasic CE images were calculated using an in-house program written in IDL (ITT Visual Information Solutions, Boulder, CO) where hepatic arterial phase begins 4 seconds after injection and the portal venous phase begins 16 seconds after injection.

Ultrasound

Ultrasound measurements were acquired with a 14-MHz linear transducer (15L8s) (Sequoia-512; Acuson, Mountain View, CA) on anesthetized mice (pentobarbital 30 mg/kg, intraperitoneally). Tumor perfusion was assessed by CE ultrasound, by intravenous injection of 150 μl of saline through the tail vein and, 5 minutes later, by intravenous injection of 150 μl of contrast medium bolus (15 mg/mouse, Definity Perflutren Lipid Microsphere; Bristol-Myers Squibb Medical Imaging, Inc, Billerica, MA). Contrast enhancement was measured for 15 seconds at a rate of 20 frames/second. For CE ultrasound analysis, the enhancement of each region of interest (ROI) was calculated from time series images using dedicated functional molecular image analysis software UIA (I-Labs, Petah-Tikva, Israel).

Image Analysis and Statistics

The number of tumors per liver and their volume assessment was performed by using Analyze 7.0 (BIR, Mayo Clinic, Rochester, MN) from the T_2W images. HRI maps were generated as reported previously [33,34] using IDL (Interactive Data Language of ITT Visual Information Solutions). For healthy mice, the selected liver ROIs covered the entire liver. For CRLM-bearing mice, tumor ROI included the entire lesion and liver ROI included representative liver tissue far away from the detected tumors as defined on the T_2W images by using the Analyze 7.0 software. Mean ΔS values were calculated from these ROI, and results are expressed as means ± SD. The difference between groups was analyzed by one-sided exact paired Student's t test for $n > 30$ data points and with one-sided exact Wilcoxon signed-rank test for a smaller sample size. Statistical analyses were performed with the Instat Biostatistics software (GraphPad Software, Inc, San Diego, CA). $P < .05$ was considered statistically significant.

Histology and Immunostaining

Mice were killed immediately after the final MRI scan, and their livers with the surrounding tissues were fixed in 4% formaldehyde for a week; the entire liver was further embedded in paraffin to preserve good correlation to MRI orientation. Finally, the livers were sliced at 1.1-mm intervals in the same axial plane as the MRI sections. The nodules that precisely corresponded to HRI (using the transverse T_2W images as a reference) were determined. These were then cut (5 μm) and stained with hematoxylin-eosin (H&E) or subjected to immunohistochemistry using anti–PECAM-1 antibodies (CD31; Biocare Medical, Concord, CA) and antibody against α-smooth muscle actin (α-SMA) (dilution 1:300; Sigma, St Louis, MO). Histologic examination was conducted by an expert hepatopathologist with more than 10 years of experience in liver pathology. The number of blood vessels was counted in 10 randomly selected high-power microscopic fields (HPF, magnification ×400) for each tumor, and the mean value ± SD was determined.

Results

CRLM Vasculature Profile Characterization by HRI

Initially, we assessed the ability of HRI to detect the vascular and perfusion changes occurring in mice with well-defined CRLM. In healthy mice, the mean liver ΔSO_2 values (the change induced by hyperoxia) were extremely positive (95% ± 18%, n = 10 livers), whereas the mean ΔSCO_2 values (the change induced by hypercapnia) were negative (–40% ± 4%, n = 10 livers; Figure 1, *A* and *D*), in agreement with the results obtained previously in rats [33]. In all the CRLM-bearing mice, the entire liver perfusion was reduced as the HRI reactivity maps for both hyperoxia and hypercapnia were significantly attenuated (62% ± 35% and –29% ± 9%, respectively, P < .001) compared with healthy liver mean values (n = 10 livers; Figure 1, *B–D*). Moreover, the ΔSO_2 and ΔSCO_2 mean values of well-defined CRLM were significantly reduced (21% ± 13% and –10% ± 7%, respectively, P < .001) compared with those of the adjacent liver (n = 30 tumors; Figure 1, *B–D*). These results may reflect hypovascularity of the CRLM nodules, with increased arterial blood supply.

CRLM Vasculature Profile Verification

Perfusion assessment methods and immunohistochemical staining were applied to evaluate vessel density and blood supply distribution of CRLM in this animal model. The hypovascularity of CRLM was clearly evident by their pale appearance compared with the reddish color of the adjacent liver parenchyma (Figure 2*A*). Furthermore, blood vessel quantization was achieved by immunohistochemical staining, with anti–PECAM-1 antibody (CD31), which confirmed the lower vessel density in CRLM compared with the dense vasculature of the liver parenchyma (Figure 2, *C* and *D*). The actual blood vessel count per HPF in healthy livers was significantly higher (35 ± 7 vessels/HPF, n = 8 livers) compared with CRLM (8 ± 3 vessels/HPF; n = 8 tumors, P < .0005). The increased arterial blood supply to CRLM in this model was assessed by using CE ultrasound (n = 3 mice). The maximum signal intensity of CRLM was lower and observed earlier than the maximum signal intensity of liver parenchyma (Figure 2*E*). Finally, by stopping Evans Blue perfusion during the arterial phase (n = 4 mice), we observed that most of the CRLM (>1 mm) turned blue, indicating their increased arterial blood supply (Figure 2*B*). These results indicate that CRLMs (>1 mm) in this animal model are indeed hypovascular and derive their vascular supply predominantly from hepatic arteries as suggested by HRI. These results from the animal model are in good agreement with the clinical knowledge regarding liver metastasis vascular properties in humans [26,27].

HRI and CE-MRI Comparison

The HRI results were further compared with multiphasic CE-MRI in this model. For CRLM with diameters ranging between 2 and 5 mm, the sensitivity of both imaging methods was high. However, the HRI method enabled detection of smaller lesions (1-2 mm) compared with the CE-MRI method. Figure 3 demonstrates an example of an image with three small foci. According to the arterial phase image and to the signal intensity–time course of CRLM *versus* liver, only one of them (marked with *red arrow*; 2. 2 mm in diameter) was enhanced, whereas the smaller lesions in this image (marked with *green arrows*; 1.6 mm in diameter) were not enhanced with Gd-DTPA (Figure 3, *E* and *G*). The HRI results of the same slice clearly delineated all three lesions (Figure 3, *B* and *C*). These results were repeated in an additional seven mice in which approximately 60% of the tumors smaller than 2 mm were not enhanced with CE-MRI.

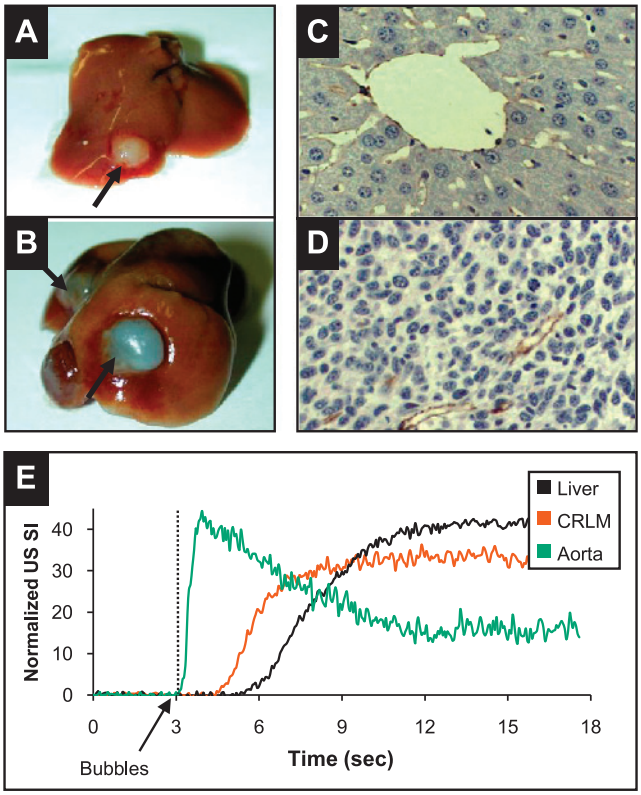

Figure 2. The hypovascularity and increased arterial blood supply of CRLM. (A) A whole liver photograph demonstrating CRLM hypovascularity (arrow). (B) Evan's Blue (EB) perfusion was stopped during the arterial phase demonstrating the increased arterial blood supply to CRLM (arrows). Endothelial immunohistochemical staining with PECAM-1 (CD31; brown stain) of healthy liver section (C) and CRLM section (D) confirmed the lower vessel density of CRLM (original magnification, ×400). (E) CE ultrasound enhancement curves from representative CRLM-bearing mouse (liver—black, CRLM—red and aorta—green; injection time is indicated on the graph). The time-intensity curves of each ROI were normalized by dividing each time point by the mean of the baseline block.

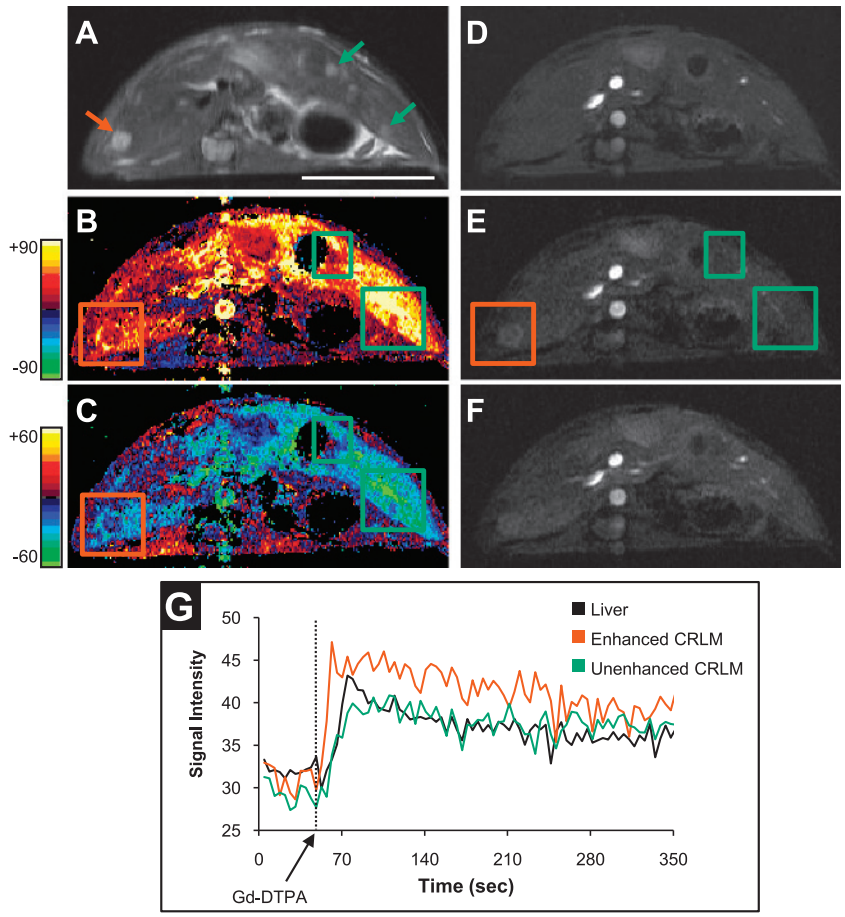

Figure 3. CRLM detectability by HRI and CE-MRI: Results from a representative mouse with several small CRLM that were analyzed with both HRI and CE-MRI. (A) Axial T_2W image with three visible CRLM (marked with arrows; bar = 1 cm). The corresponding HRI maps of the same slice (B—ΔS_{O_2} map; C—ΔS_{CO_2} map). Color scales for ΔS maps are located on the left. All three lesions were clearly visible with HRI. The multiphasic CE T_1W images that were obtained before (D) and 13.2 seconds (E; arterial phase) and 26.4 seconds (F; portal phase) after Gd-DTPA injection. Only the largest CRLM (marked with red box; 2.2 mm in diameter) was enhanced during the arterial phase, whereas the smaller lesions (marked with green boxes; 1.6 mm) were not enhanced during the arterial phase. (G) CE-MRI signal intensity–time curves measured from the same mouse of liver parenchyma (black), the enhanced CRLM (red), and the unenhanced CRLM (green). The injection time is indicated on the graph.

We further extended the sample size by including additional mice that were scanned with only one of the perfusion methods (either HRI or CE-MRI). The sensitivity results of lesion-by-lesion analysis for both HRI and CE-MRI are given in Table 1. In this animal model, the sensitivity for small CRLM detection (1-2 mm in diameter) of CE-MRI (n = 21 lesions) was 38%, whereas the sensitivity of the HRI method was higher 82% (n = 17 lesions). For larger CRLM lesions (between 2 and 5 mm in diameter), the sensitivity improved considerably for both methods, whereas CE-MRI showed a sensitivity of 81% (17/21); the HRI sensitivity was 97% (29/30).

Assessment of the Vascular Changes during Advanced CRLM Progression

To characterize the changes in tumor perfusion during CRLM progression, advanced CRLM (≥7 mm in diameter) were assessed by HRI (n = 6 tumors). Along with tumor growth, the center of these tumors appeared hyperintense in T_2W images, an appearance that could reflect development of necrosis (Figure 4*A*). When we analyzed the corresponding HRI maps, ΔS_{O_2} values were significantly positive at the center of these tumors (37% ± 13%, P < .01) compared with the outer CRLM region values (Figure 4, *B* and *D*), suggesting increased vascular density and blood content. Moreover, the ΔS_{CO_2} values became significantly negative (–27% ± 6%, P < .01) compared with the outer CRLM region values (Figure 4, *C* and *D*). In addition, the HRI values at the center of these tumors were also significantly different compared with those of the adjacent liver parenchyma HRI (P < .05; Figure 4*D*). Indeed, H&E staining and immunohistochemical staining with anti–PECAM-1 antibody (CD31) and α-SMA antibody revealed highly arborized and widened matured blood vessels at the center of

Table 1. Sensitivity Results of Lesion-by-Lesion Analysis.

CRLM Diameter (mm)	No. Detected (True Positive)	No. Missed (False Negative)	Sensitivity (%)
(A) HRI results			
1 ≤ t < 2 mm	14	3	82
2 ≤ t < 5 mm	29	1	97
(B) CE-MRI results			
1 ≤ t < 2 mm	8	13	38
2 ≤ t < 5 mm	17	4	81

these tumors, reinforcing the HRI findings regarding increased vascularity at the center of these advanced tumors (Figure 4, *E–G*).

Assessment of the Vascular Changes during RAPA Therapy

To assess the use of HRI for antiangiogenic treatment evaluation, we treated CRLM-bearing mice with RAPA. CRLM growth was delayed by 8 days in average in the RAPA-treated mice. The HRI response to both hyperoxia and hypercapnia of CRLM in RAPA-treated mice was significantly attenuated compared with control-treated CRLM (Figure 5, *A–C*; $n = 13$ tumors; $P < .05$), whereas the liver HRI values were similar to those measured from untreated mice. Surprisingly, at the center of RAPA-treated CRLM, areas with positive ΔS_{CO_2} were detected (Figure 5*B*). Blood vessel quantization (by immunohistochemical staining, with anti–PECAM-1 antibody) showed reduced vessel density in RAPA-treated CRLM (6 ± 1.3 vessels/HPF $n = 9$ tumors) compared with control-treated CRLM (9 ± 1.9 vessels/HPF $n = 8$ tumors, $P < .005$), in agreement with the HRI map attenuation. Furthermore, most of the vessels at the center of the RAPA-treated tumors were widened (Figure 5, *G* and *H*), clarifying the positive ΔS_{CO_2} values detected in these tumors. When analyzing vessel maturation status in these CRLMs, we noticed that most of the vessels were stained with α-SMA both in the RAPA-treated and untreated tumors (Figure 5, *F* and *I*). In addition, there were areas with reduced tumor cell density at the center of RAPA-treated CRLM (Figure 5*H*).

Vascular Profile Assessment of Primary Hepatic Lesions

To evaluate the HRI utility to study the vascular profile of primary hepatic lesions, we used *Mdr2* knockout mice as the animal model [37]. We compared the HRI findings with the routinely used T_1W, T_2W, CE-MRI, and histologic evaluation ($n = 21$ lesions). On T_2W images, the detected lesions were either hyperintense or isointense. Most of these lesions were also isointense on precontrast T_1W images (see examples in Figure 6*A*). With CE-MRI, only some of the suspected lesions were enhanced either with central enhanced foci (Figure 6, *B* and *C*) or at the periphery of the lesion (Figure 6*D*). The HRI method revealed three distinct patterns of responses: 1) heterogeneous HRI response with regions of high response and others with a slightly reduced response (see example in Figure 6*B*), 2) elevated HRI response covering the entire lesion (see example in Figure 6*C*), and 3) significantly reduced HRI response compared with the adjacent inflamed liver with high ΔS values at the periphery (see example in Figure 6*D*). The pathologic identification, obtained from the

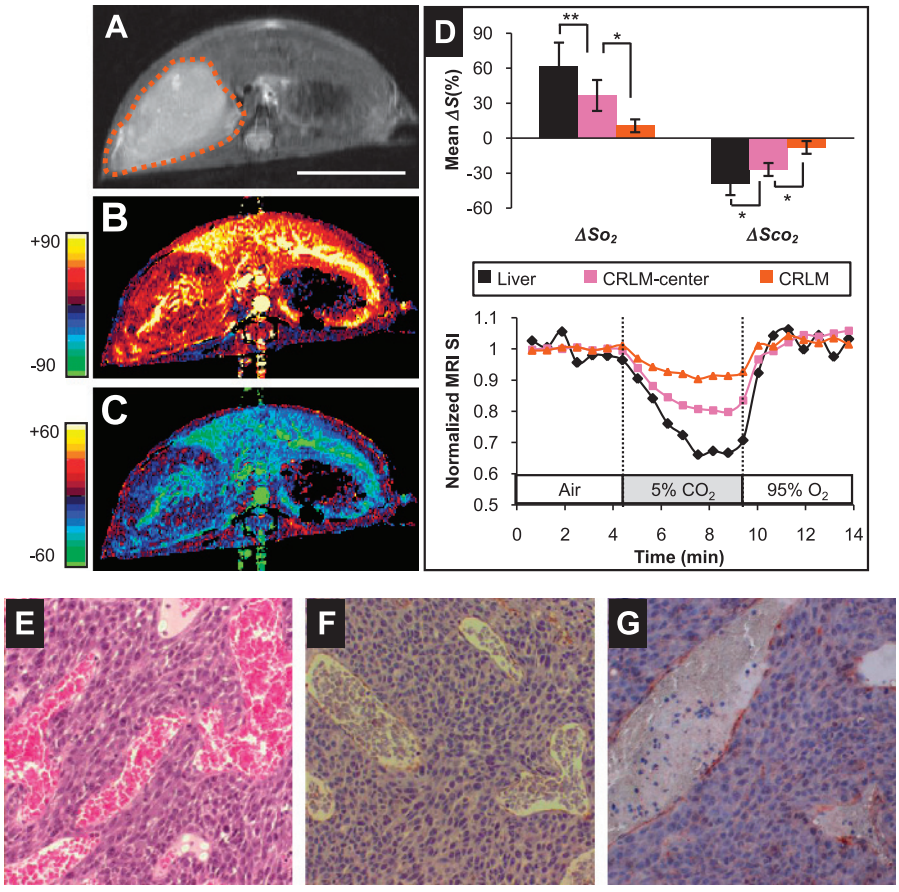

Figure 4. HRI analysis of advanced CRLM. (A) Axial T_2W image of a mouse with advanced CRLM (encircled, 25 days after cell injection; bar = 1 cm) and the corresponding HRI maps (B—ΔS_{O_2} map; C—ΔS_{CO_2} map) of the same slice. Color scales for ΔS maps are located on the left. The center of the tumor showed atypical HRI reactivity maps. (D) (top) Mean ΔS_{O_2} and ΔS_{CO_2} values ± SD of healthy liver parenchyma (black), of central regions in advanced CRLM (pink), and of the outer regions in advanced CRLM (red) ($n = 6$ tumors): $^*P < .01$ and $^{**}P < .05$. (bottom) Representative HRI time courses obtained from this mouse, of liver tissue (black), from the center of advanced CRLM (pink), and of the outer CRLM region (red). Relevant histologic slides were stained with H&E staining (E), and immunohistochemical staining with PECAM-1 (F; brown stain) for endothelial cells and with α-SMA (G; red stain) for smooth muscle cells revealed highly arborized matured blood vessels (original magnification, ×200) at the center of these tumors.

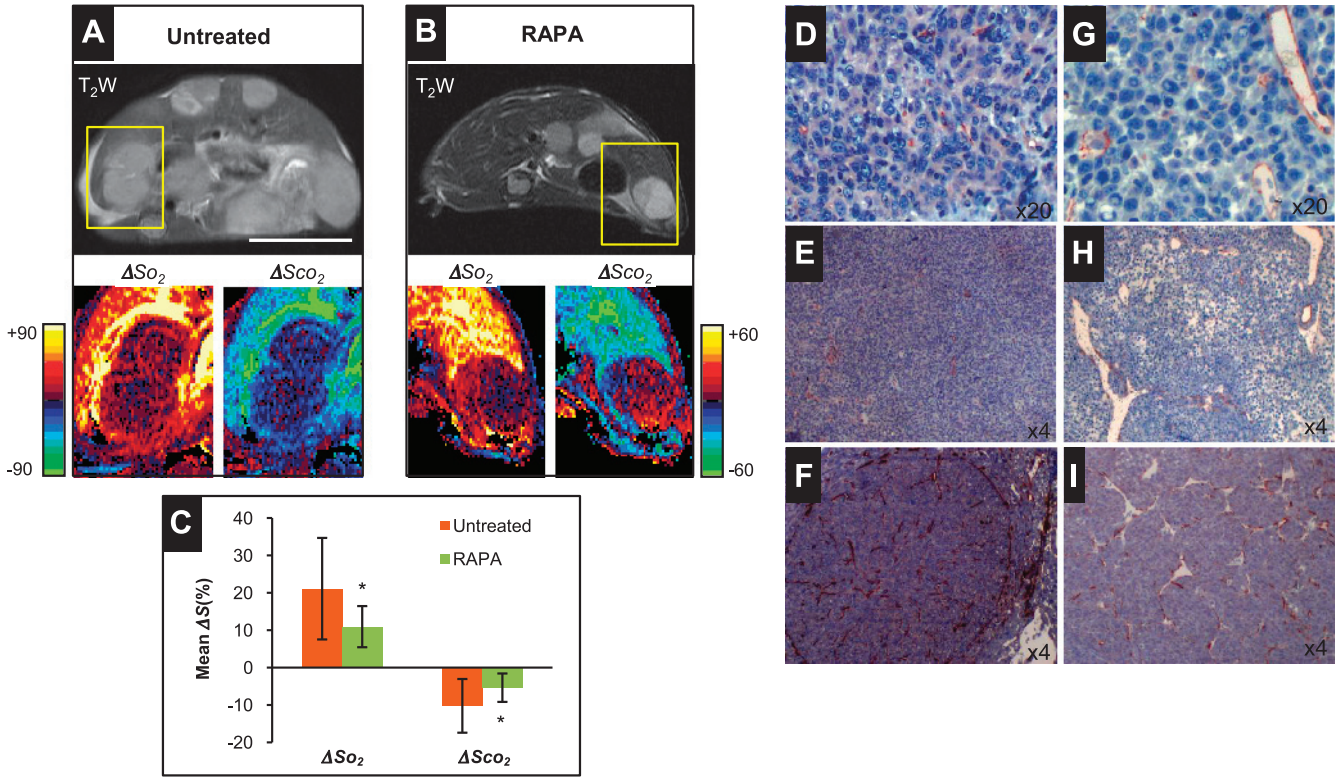

Figure 5. The vascular changes during RAPA therapy. (A and B) Representatives axial T_2W images (top) and enlarged HRI maps of the marked tumors (bottom) of control-treated mouse (A) and RAPA-treated mouse (B). Bar = 1 cm (A). Color scales for ΔS maps are located on both sides. (C) Mean ΔS_{O_2} and ΔS_{CO_2} values ± SD of control-treated CRLM (red; n = 30 tumors) and RAPA-treated CRLM (green; n = 13 tumors): $^*P < .05$. The ΔS_{CO_2} maps of RAPA-treated tumors showed pixels with positive reactivity to hypercapnia differing from control-treated CRLM. Relevant histologic slides were immunohistochemically stained with PECAM-1 (CD31—red stain; D, E, G, H) for endothelial cells or with α-SMA (F, I; red stain) for smooth muscle cells (original magnification, ×200 [D, G], ×40 [E, F, H, I]). CD31 staining demonstrated widened blood vessels at the center of the RAPA-treated tumors. Anti–α-SMA staining confirmed that most of the tumor vessels were covered with smooth muscle cells, explaining the moderate antiangiogenic effect of RAPA on these CRLMs.

corresponding histologic sections, could distinguish between poorly differentiated HCC (pattern I, n = 11 lesions; Figure 6*B*), well-differentiated HCC (pattern II, n = 6 lesions; Figure 6*C*), and necrotic/cystic foci (pattern III, n = 7 lesions; Figure 6*D*). There was a good correlation between the HRI classification and the pathologic differentiation, which may imply a beneficial usage of HRI as a complementary method for the assessment of the vascular profile of suspected primary hepatic lesions.

Discussion

The widespread use of modern imaging techniques increases the detection of liver tumors. Early detection of liver malignancies, new therapeutic options, and new monitoring methods may improve treatment outcome. Reliable noninvasive characterization and differentiation of these lesions are of utmost importance for clinical practice [38]. In primary and metastatic liver malignancies, there is a relative increase in arterial blood supply to the tumor [26,27]. Perfusion imaging has been suggested to improve the sensitivity and specificity of liver tumor diagnostics [27]. It is well accepted that CE imaging techniques can improve the diagnosis of liver lesions larger than 1 cm [38,39] by showing increased arterial blood supply to the tumor with venous washout. Nevertheless, even the optimized imaging techniques remain relatively insensitive for the detection and vascular characterization studies of smaller nodules. In this research, we demonstrated the applicability of HRI, an fMRI method combined with hypercapnia and hyperoxia, for liver tumor vascular characterization. By using HRI, the hemodynamic changes occurring during CRLM establishment were detected, thus enabling classification of suspected foci with high sensitivity. In addition, the HRI method demonstrated the vascular changes induced by RAPA treatment and facilitated primary hepatic tumor characterization with good correlation to the pathologic differentiation.

Recently, we reported the applicability of HRI for monitoring changes in liver perfusion and hemodynamics during liver regeneration, fibrosis, and acute bleeding in rat models, without the need of contrast agent administration [34,35]. We demonstrated that during CO_2 enrichment, there is an increase in portal blood flow to the liver [33]. The resultant higher deoxyhemoglobin levels produced a decrease in fMRI signal intensity, which is illustrated by negative ΔS_{CO_2} values. Thus, liver ΔS_{CO_2} values are sensitive to changes in the ratio between the portal and arterial blood supplies. The signal change induced by hyperoxia signifies vascular density and tissue perfusion [33,40].

In this study, we demonstrated that, in mice, CRLM have distinctive HRI reactivity maps compared with those obtained from healthy livers. The reduction of negative ΔS_{CO_2} values in response to hypercapnia is extremely sensitive to both tumor hypovascularity and to the increased arterial blood supply occurring during CRLM progression. The decreased ΔS_{O_2} values in response to hyperoxia emphasize the hypovascularity of CRLM nodules. Moreover, HRI values of

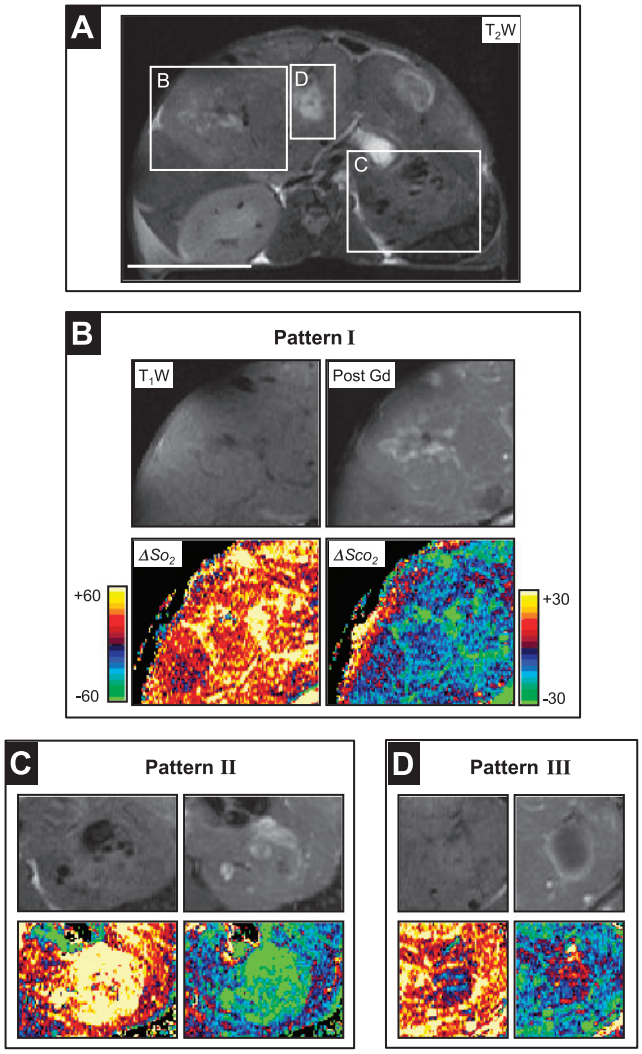

Figure 6. Primary hepatic lesions vascular characterization by HRI: Three distinct patterns of HRI responses were observed in hepatic lesions identified in elderly *Mdr2* knockout mice. (A) Representative T_2W image of a 17-month-old *Mdr2*-knockout mouse on which three different lesions are marked with white rectangles (bar = 1 cm). (B–D) Each panel represents one pattern and contains the corresponding enlarged T_1W images obtained before and after Gd injection (Top), and the corresponding enlarged HRI maps (bottom, left—ΔS_{O_2} map; right—ΔS_{CO_2} map; color scale for ΔS maps is shown on B). (B) Representative sample for pattern I—with heterogeneous HRI response that was found to be characteristic for poorly differentiated HCC. (C) Representative example for pattern II—with homogeneously elevated HRI response that was found to be distinctive for well-differentiated HCC. (D) Representative sample of pattern III—with reduced HRI response inside the lesion with high ΔS values at the periphery that was found to be distinctive for necrotic foci.

healthy livers were significantly higher compared with those from livers of CRLM-bearing mice. This phenomenon may be explained by the notion that, in the presence of overt CRLM, a higher proportion of liver blood flow is derived from the hepatic artery, thus changing the entire liver hemodynamic in CRLM-bearing mice [28,41]. The CRLM mouse model used in this study revealed vascular alterations and pathologic appearance similar to those detected in human CRLM [42]. However, the rate of tumor progression in this model was faster than the kinetics known in CRLM patients.

In the described CRLM animal model, the sensitivity to detect small metastases (1-2 mm) by using HRI was significantly higher (82%) compared with multiphasic CE-MRI (38%). Previous studies showed that small CRLM (<520 μm) are hypovascular [42], and only advanced CRLM (>2000 μm) showed an exclusively arterial blood supply [42,43]. This observation may explain the enhanced detectability of HRI compared with multiphasic CE-MRI. Whereas multiphasic CE-MRI detects only the increased arterial blood supply of CRLM, HRI could also demonstrate the reduced vessel density occurring during the early phases of CRLM progression. Furthermore, the use of contrast agents, in both CT and MRI, could be associated with nephrotoxicity, especially in patients with risk factors such as renal failure, vascular disease, and diabetes [44]. The HRI method may provide a safer alternative for these patients.

The high sensitivity of HRI for small CRLM and the spatial information derived from these maps were further used to classify suspected CRLM lesions in their early growth phase by using a machine learning approach [45] (Figure W1). We showed that the recall (sensitivity) and precision (equal to positive predictive value) of HRI for suspected CRLM confirmation (≤1.6 mm) were 77% and 88%, respectively. The ability to detect subtle hemodynamic changes during CRLM establishment can assist to understand the metastasis development and progression mechanism and to develop drugs directed to the early growth phase.

Identification of new noninvasive monitoring techniques for assessing early tumor response to therapy is a major need and could facilitate decisions regarding therapy continuation or replacement. The assessment of RAPA treatment effect by HRI revealed alterations in CRLM vasculature growth pattern that were further confirmed by histologic findings. Whereas the RAPA therapy reduced tumor vascularity, it also caused the swelling of the remaining vessels. By immunostaining for α-SMA, we confirmed that most of these vessels were covered with smooth muscle cells, thus explaining the moderate antiangiogenic effect of RAPA on these CRLMs. The HRI results revealed differences between the vasculature properties at the center of RAPA-treated CRLM and the center of advanced CRLM lesions (≥7 mm). These differences were further confirmed by histologic evaluation. All of these findings emphasized the potency of HRI for understanding the underling mechanism of antiangiogenic drugs with the goal of developing strategies that could lead to earlier evaluation of the therapeutic efficacy noninvasively.

The detection and characterization of primary hepatic nodules in the multistage development of HCC in a cirrhotic liver remain an important challenge for clinicians [30,31]. We assessed the potential of HRI for HCC diagnosis based on the functional vascular profile of a variety of hepatic lesions in the *Mdr2* knockout mouse model [37]. By using HRI, we could distinguish three distinct patterns of responses to the inhaled gases, which were in good correlation to the pathologic diagnosis. These results imply that HRI may facilitate the differentiation between different types of hepatic lesions based on their vascular profile noninvasively.

There are several limitations to the current study. First, liver fMRI in humans can be limited by respiratory motion artifact, which may reduce measurement accuracy and is very critical for achieving significant ΔS maps. Respiratory motion artifacts can be suppressed by navigator-gated methods [46] or corrected by postacquisition processing [47]. Because our experiments were performed on anesthetized mice, most of the motion artifacts were negligible, and there was no need for additional data processing. Second, our HRI method is

based on T_2*-weighted images that are very sensitive to in-homogeneity and could be very susceptible to intrasubject and intersubject variability. To avoid this variability and to improve HRI reproducibility, we assessed the potential usage of R_2* maps during hyperoxia and hypercapnia challenges for CRLM detection in mice. Our preliminary results illustrate that the HRI and ΔR_2* maps yield similar qualitative results (Figure W2), suggesting that dynamic measurement may not be required, thus permitting improved spatial resolution. Indeed, the use of R_2* maps in 3-T clinical MR machine for liver fibrosis assessment with carbogen challenge was recently demonstrated [48]. Finally, our experiments were performed on animal models, and although the models resemble the human disease, promising results of HRI for liver tumor detection should be further investigated and reproduced in patients with liver tumors.

In summary, HRI offers a new technique to monitor changes of vessel density and perfusion ratio in liver tumors noninvasively without the need for contrast agent administration. Our experimental data from mice provide comprehensive evidence for the use of this method for earlier and more accurate hepatic tumor diagnosis in both primary and metastatic tumors. In addition, this method can serve as an imaging tool for the study of the underling mechanism of antiangiogenic drugs based on the results regarding vascular alterations during RAPA treatment. We believe that, by combining HRI with the well-established perfusion imaging methods (CE-MRI, etc), hepatic tumor detection and therapy monitoring could be improved.

Acknowledgments

The authors thank Evelyne Zeira for her helpful assistance with the CRLM model establishment and Mery Clausen for article editing.

References

[1] El-Serag HB and Rudolph KL (2007). Hepatocellular carcinoma: epidemiology and molecular carcinogenesis. *Gastroenterology* **132**, 2557–2576.

[2] Llovet JM and Bruix J (2008). Novel advancements in the management of hepatocellular carcinoma in 2008. *J Hepatol* **48**(Suppl 1), S20–S37.

[3] Baker ME and Pelley R (1995). Hepatic metastases: basic principles and implications for radiologists. *Radiology* **197**, 329–337.

[4] Jemal A, Siegel R, Ward E, Hao Y, Xu J, Murray T, and Thun MJ (2008). Cancer statistics, 2008. *CA Cancer J Clin* **58**, 71–96.

[5] McLoughlin JM, Jensen EH, and Malafa M (2006). Resection of colorectal liver metastases: current perspectives. *Cancer Control* **13**, 32–41.

[6] El-Serag HB, Marrero JA, Rudolph L, and Reddy KR (2008). Diagnosis and treatment of hepatocellular carcinoma. *Gastroenterology* **134**, 1752–1763.

[7] Finlay IG and McArdle CS (1983). Effect of occult hepatic metastases on survival after curative resection for colorectal carcinoma. *Gastroenterology* **85**, 596–599.

[8] Rothbarth J and van de Velde CJ (2005). Treatment of liver metastases of colorectal cancer. *Ann Oncol* **16**(Suppl 2), ii144–ii149.

[9] Ruers T and Bleichrodt RP (2002). Treatment of liver metastases, an update on the possibilities and results. *Eur J Cancer* **38**, 1023–1033.

[10] Vogl TJ, Zangos S, Eichler K, Yakoub D, and Nabil M (2007). Colorectal liver metastases: regional chemotherapy via transarterial chemoembolization (TACE) and hepatic chemoperfusion: an update. *Eur Radiol* **17**, 1025–1034.

[11] Semela D, Piguet AC, Kolev M, Schmitter K, Hlushchuk R, Djonov V, Stoupis C, and Dufour JF (2007). Vascular remodeling and antitumoral effects of mTOR inhibition in a rat model of hepatocellular carcinoma. *J Hepatol* **46**, 840–848.

[12] Guba M, von Breitenbuch P, Steinbauer M, Koehl G, Flegel S, Hornung M, Bruns CJ, Zuelke C, Farkas S, Anthuber M, et al. (2002). Rapamycin inhibits primary and metastatic tumor growth by antiangiogenesis: involvement of vascular endothelial growth factor. *Nat Med* **8**, 128–135.

[13] Luan FL, Ding R, Sharma VK, Chon WJ, Lagman M, and Suthanthiran M (2003). Rapamycin is an effective inhibitor of human renal cancer metastasis. *Kidney Int* **63**, 917–926.

[14] Hojo M, Morimoto T, Maluccio M, Asano T, Morimoto K, Lagman M, Shimbo T, and Suthanthiran M (1999). Cyclosporine induces cancer progression by a cell-autonomous mechanism. *Nature* **397**, 530–534.

[15] Luan FL, Hojo M, Maluccio M, Yamaji K, and Suthanthiran M (2002). Rapamycin blocks tumor progression: unlinking immunosuppression from antitumor efficacy. *Transplantation* **73**, 1565–1572.

[16] Brindle K (2008). New approaches for imaging tumour responses to treatment. *Nat Rev Cancer* **8**, 94–107.

[17] Michaelis LC and Ratain MJ (2006). Measuring response in a post-RECIST world: from black and white to shades of grey. *Nat Rev Cancer* **6**, 409–414.

[18] Miller JC, Pien HH, Sahani D, Sorensen AG, and Thrall JH (2005). Imaging angiogenesis: applications and potential for drug development. *J Natl Cancer Inst* **97**, 172–187.

[19] Checkley D, Tessier JJ, Kendrew J, Waterton JC, and Wedge SR (2003). Use of dynamic contrast-enhanced MRI to evaluate acute treatment with ZD6474, a VEGF signalling inhibitor, in PC-3 prostate tumours. *Br J Cancer* **89**, 1889–1895.

[20] Drevs J, Muller-Driver R, Wittig C, Fuxius S, Esser N, Hugenschmidt H, Konerding MA, Allegrini PR, Wood J, Hennig J, et al. (2002). PTK787/ZK 222584, a specific vascular endothelial growth factor-receptor tyrosine kinase inhibitor, affects the anatomy of the tumor vascular bed and the functional vascular properties as detected by dynamic enhanced magnetic resonance imaging. *Cancer Res* **62**, 4015–4022.

[21] Evelhoch JL, LoRusso PM, He Z, DelProposto Z, Polin L, Corbett TH, Langmuir P, Wheeler C, Stone A, Leadbetter J, et al. (2004). Magnetic resonance imaging measurements of the response of murine and human tumors to the vascular-targeting agent ZD6126. *Clin Cancer Res* **10**, 3650–3657.

[22] Fuh G, Wu P, Liang WC, Ultsch M, Lee CV, Moffat B, and Wiesmann C (2006). Structure-function studies of two synthetic anti–vascular endothelial growth factor Fabs and comparison with the Avastin Fab. *J Biol Chem* **281**, 6625–6631.

[23] Mross K, Drevs J, Muller M, Medinger M, Marme D, Hennig J, Morgan B, Lebwohl D, Masson E, Ho YY, et al. (2005). Phase I clinical and pharmacokinetic study of PTK/ZK, a multiple VEGF receptor inhibitor, in patients with liver metastases from solid tumours. *Eur J Cancer* **41**, 1291–1299.

[24] Barrett T, Brechbiel M, Bernardo M, and Choyke PL (2007). MRI of tumor angiogenesis. *J Magn Reson Imaging* **26**, 235–249.

[25] Leach MO, Brindle KM, Evelhoch JL, Griffiths JR, Horsman MR, Jackson A, Jayson GC, Judson IR, Knopp MV, Maxwell RJ, et al. (2005). The assessment of antiangiogenic and antivascular therapies in early-stage clinical trials using magnetic resonance imaging: issues and recommendations. *Br J Cancer* **92**, 1599–1610.

[26] Breedis C and Young G (1954). The blood supply of neoplasms in the liver. *Am J Pathol* **30**, 969–977.

[27] Pandharipande PV, Krinsky GA, Rusinek H, and Lee VS (2005). Perfusion imaging of the liver: current challenges and future goals. *Radiology* **234**, 661–673.

[28] Leveson SH, Wiggins PA, Giles GR, Parkin A, and Robinson PJ (1985). Deranged liver blood flow patterns in the detection of liver metastases. *Br J Surg* **72**, 128–130.

[29] Leen E, Goldberg JA, Angerson WJ, and McArdle CS (2000). Potential role of Doppler perfusion index in selection of patients with colorectal cancer for adjuvant chemotherapy. *Lancet* **355**, 34–37.

[30] Bruix J, Sherman M, Llovet JM, Beaugrand M, Lencioni R, Burroughs AK, Christensen E, Pagliaro L, Colombo M, and Rodes J (2001). Clinical management of hepatocellular carcinoma. Conclusions of the Barcelona-2000 EASL conference. European Association for the Study of the Liver. *J Hepatol* **35**, 421–430.

[31] Bruix J and Sherman M (2005). Management of hepatocellular carcinoma. *Hepatology* **42**, 1208–1236.

[32] Coenegrachts K, Ghekiere J, Denolin V, Gabriele B, Herigault G, Haspeslagh M, Daled P, Bipat S, Stoker J, and Rigauts H (2010). Perfusion maps of the whole liver based on high temporal and spatial resolution contrast-enhanced MRI (4D THRIVE): feasibility and initial results in focal liver lesions. *Eur J Radiol* **74**, 529–535.

[33] Barash H, Gross E, Matot I, Edrei Y, Tsarfaty G, Spira G, Vlodavsky I, Galun E, and Abramovitch R (2007). Functional MR imaging during hypercapnia and hyperoxia: noninvasive tool for monitoring changes in liver perfusion and hemodynamics in a rat model. *Radiology* **243**, 727–735.

[34] Barash H, Gross E, Edrei Y, Pappo O, Spira G, Vlodavsky I, Galun E, Matot I, and Abramovitch R (2008). Functional magnetic resonance imaging monitoring of pathological changes in rodent livers during hyperoxia and hypercapnia. *Hepatology* **48**, 1232–1241.

[35] Matot I, Cohen K, Pappo O, Barash H, and Abramovitch R (2008). Liver response to hemorrhagic shock and subsequent resuscitation: MRI analysis. *Shock* **29**, 16–24.

[36] Kollmar O, Schilling MK, and Menger MD (2004). Experimental liver metastasis: standards for local cell implantation to study isolated tumor growth in mice. *Clin Exp Metastasis* **21**, 453–460.

[37] Mauad TH, van Nieuwkerk CM, Dingemans KP, Smit JJ, Schinkel AH, Notenboom RG, van den Bergh Weerman MA, Verkruisen RP, Groen AK, Oude Elferink RP, et al. (1994). Mice with homozygous disruption of the *mdr2* P-glycoprotein gene. A novel animal model for studies of nonsuppurative inflammatory cholangitis and hepatocarcinogenesis. *Am J Pathol* **145**, 1237–1245.

[38] Robinson PJ (2000). Imaging liver metastases: current limitations and future prospects. *Br J Radiol* **73**, 234–241.

[39] Blyth S, Blakeborough A, Peterson M, Cameron IC, and Majeed AW (2008). Sensitivity of magnetic resonance imaging in the detection of colorectal liver metastases. *Ann R Coll Surg Engl* **90**, 25–28.

[40] Abramovitch R, Frenkiel D, and Neeman M (1998). Analysis of subcutaneous angiogenesis by gradient echo magnetic resonance imaging. *Magn Reson Med* **39**, 813–824.

[41] Leen E (1999). The detection of occult liver metastases of colorectal carcinoma. *J Hepatobiliary Pancreat Surg* **6**, 7–15.

[42] Liu Y and Matsui O (2007). Changes of intratumoral microvessels and blood perfusion during establishment of hepatic metastases in mice. *Radiology* **243**, 386–395.

[43] Dezso K, Bugyik E, Papp V, Laszlo V, Dome B, Tovari J, Timar J, Nagy P, and Paku S (2009). Development of arterial blood supply in experimental liver metastases. *Am J Pathol* **175**, 835–843.

[44] ten Dam MA and Wetzels JF (2008). Toxicity of contrast media: an update. *Neth J Med* **66**, 416–422.

[45] Freiman M, Edrei Y, Sela Y, Shmidmayer Y, Gross E, Joskowicz L, and Abramovitch R (2008). Classification of suspected liver metastases using fMRI images: a machine learning approach. *Med Image Comput Comput Assist Interv* **11**, 93–100.

[46] Song R, Cohen AR, and Song HK (2007). Improved transverse relaxation rate measurement techniques for the assessment of hepatic and myocardial iron content. *J Magn Reson Imaging* **26**, 208–214.

[47] White MJ, Hawkes DJ, Melbourne A, Collins DJ, Coolens C, Hawkins M, Leach MO, and Atkinson D (2009). Motion artifact correction in free-breathing abdominal MRI using overlapping partial samples to recover image deformations. *Magn Reson Med* **62**, 440–449.

[48] Jin N, Deng J, Chadashvili T, Zhang Y, Guo Y, Zhang Z, Yang GY, Omary RA, and Larson AC (2010). Carbogen gas-challenge BOLD MR imaging in a rat model of diethylnitrosamine-induced liver fibrosis. *Radiology* **254**, 129–137.

Supplementary Methods

ΔR_2 Maps*

Multigradient echo (MGRE) was used to quantify the transverse relaxation rate R_2*, with a repetition time of 200 milliseconds, an initial echo time of 5 milliseconds, an echo time spacing of 5 milliseconds, 5 echo times, flip angle $\alpha = 40$ degrees, and 2 averages. The total imaging time was approximately 3.5 minutes. Three sets of MGRE images were acquired: 1) during breathing air, 2) after 3 minutes of 5% CO_2 breathing (4 L/min) through a mask, and 3) after a 3-minute carbogen breathing (4 L/min).

Liver R_2* (=1/T_2*) maps for each slice were generated from the MGRE images on a pixel-by-pixel basis by standard least square fitting of the natural log of the signal intensity *versus* TE [1], for the three inhaled gases. $\Delta R^*_{CO_2}$ was calculated by subtracting R_2*-CO_2 map from R_2*-air map, and $\Delta R^*_{O_2}$ was calculated by subtracting R_2*-CO_2 map from R_2*-O_2 map [2].

Supplementary References

[1] Song R, Cohen AR, and Song HK (2007). Improved transverse relaxation rate measurement techniques for the assessment of hepatic and myocardial iron content. *J Magn Reson Imaging* **26**, 208–214.

[2] Jin N, Deng J, Chadashvili T, Zhang Y, Guo Y, Zhang Z, Yang GY, Omary RA, and Larson AC (2010). Carbogen gas-challenge BOLD MR imaging in a rat model of diethylnitrosamine-induced liver fibrosis. *Radiology* **254**, 129–137.

[3] Freiman M, Edrei Y, Sela Y, Shmidmayer Y, Gross E, Joskowicz L, and Abramovitch R (2008). Classification of suspected liver metastases using fMRI images: a machine learning approach. *Med Image Comput Comput Assist Interv* **11**, 93–100.

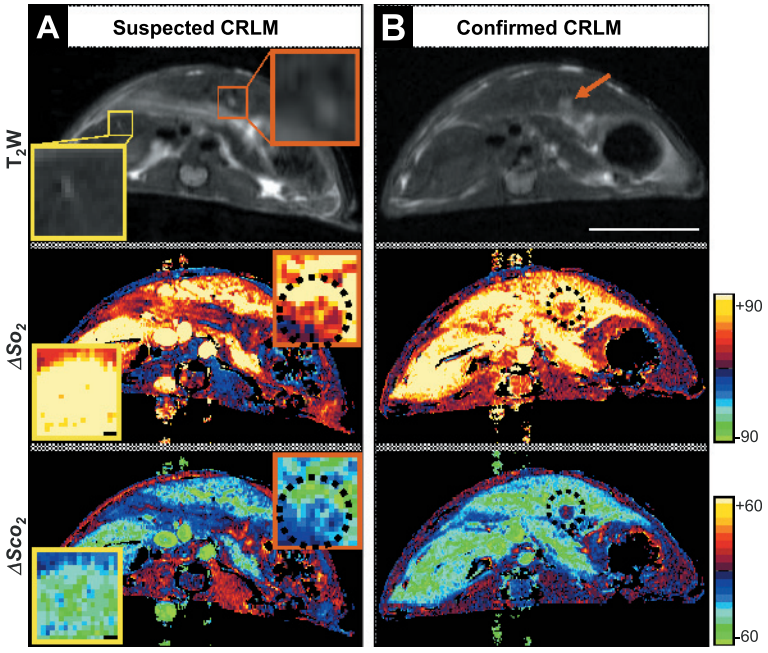

Figure W1. HRI accuracy for suspected CRLM detection: (A) Axial T_2W images (top) and HRI maps of ΔS_{O_2} (center) and ΔS_{CO_2} (bottom) of a representative mouse with two suspected CRLM, acquired 14 days after cell injection (A, enlarged squares, ×3) and 4 days later (B). Only one suspected focal lesion (red square) was classified as CRLM by HRI using a machine learning approach [3] (A) and was later confirmed by standard MRI follow-up (B, red arrow and circles). Bar = 1 cm applies for all images. Color scale for ΔS maps are located on the right.

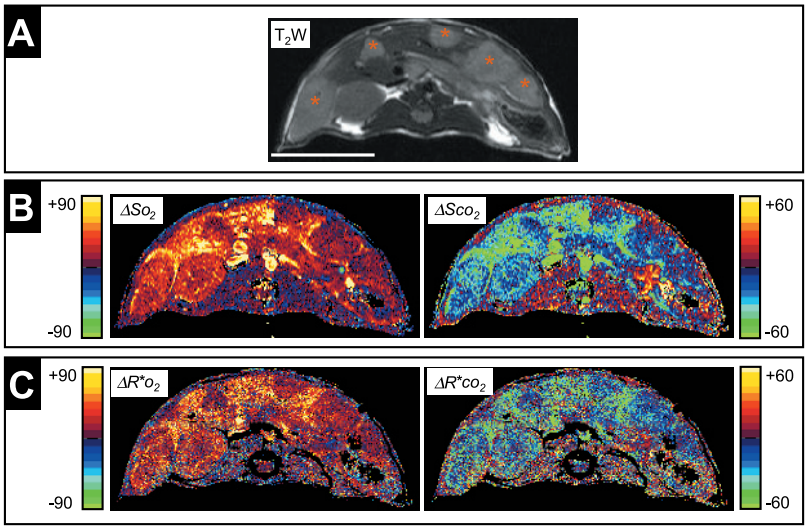

Figure W2. HRI *versus* ΔR_2*: Comparison between HRI maps and ΔR_2* maps obtained from a CRLM-bearing mouse. (A) Axial T_2W image with five CRLM nodules (marked with red asterisks). (B) The corresponding ΔS_{O_2} map (left) and ΔS_{CO_2} map (right). (C) The corresponding $\Delta R^*_{O_2}$ map (left) and $\Delta R^*_{CO_2}$ map (right). Bar = 1 cm in A and applies to all images. Color scale for ΔS and ΔR* maps are located on the left (for hyperoxia) and right (for hypercapnia) [3].